applied sciences

MDPI

Article

Effect of Micro Solidification Crack on Mechanical Performance of Remote Laser Welded AA6063-T6 Fillet Lap Joint in Automotive Battery Tray Construction

Tianzhu Sun [1,*], Pasquale Franciosa [1], Conghui Liu [2], Fabio Pierro [1] and Dariusz Ceglarek [1]

[1] Warwick Manufacturing Group (WMG), University of Warwick, Coventry CV4 7AL, UK; P.Franciosa@warwick.ac.uk (P.F.); fabiopierro91@gmail.com (F.P.); D.J.Ceglarek@warwick.ac.uk (D.C.)
[2] School of Materials, The University of Manchester, Manchester M13 9PL, UK; Conghui.liu@postgrad.manchester.ac.uk
* Correspondence: Tianzhu.sun@warwick.ac.uk

Abstract: Remote laser welding (RLW) has shown a number of benefits of joining 6xxx aluminium alloys such as high processing speed and process flexibility. However, the crack susceptibility of 6xxx aluminium alloys during RLW process is still an open problem. This paper experimentally assesses the impact of transverse micro cracks on joint strength and fatigue durability in remote laser welding of extruded AA6063-T6 fillet lap joints. Distribution and morphology of transverse micro cracks were acquired by scanning electron microscope (SEM) on cross-sections. Grain morphology in the weld zone was determined by electron backscatter diffraction (EBSD) while static tensile and dynamic fatigue tests were carried out to evaluate weld mechanical performance. Results revealed that increasing welding speed from 2 m/min to 6 m/min did not introduce additional transverse micro cracks. Additionally, welding at 2 m/min resulted in tensile strength improvement by 30% compared to 6 m/min due to the expansion of fusion zone, measured by the throat thickness, and refinement of columnar grains near fusion lines. Furthermore, the weld fatigue durability is significantly higher when fracture occurs in weld root instead of fusion zone. This can be achieved by increasing weld root angle with optimum weld fatigue durability at around 55°.

Keywords: battery tray; remote laser welding; micro solidification cracks; beam oscillation; power modulation; joint integrity

Citation: Sun, T.; Franciosa, P.; Liu, C.; Pierro, F.; Ceglarek, D. Effect of Micro Solidification Crack on Mechanical Performance of Remote Laser Welded AA6063-T6 Fillet Lap Joint in Automotive Battery Tray Construction. *Appl. Sci.* **2021**, *11*, 4522. https://doi.org/10.3390/app11104522

Academic Editor: Alberto Campagnolo

Received: 15 April 2021
Accepted: 7 May 2021
Published: 15 May 2021

1. Introduction

Battery tray is a core component of battery electric vehicles (BEVs) and plug-in hybrid electric vehicles (PHEVs) for housing battery modules and packs, and for providing the mechanical interface between vehicle body structure and the road [1]. Its design implies a high level of engineering complexity with multiple requirements such as water/gas tightness, weight minimisation and inclusion of thermal management system. At the same time, it acts as a structural component which must satisfy crash protection requirements for vehicle and occupant safety. The selection of materials and joining process for assembly of battery tray is crucial and must satisfy key performance indicators at design, as mentioned above, as well as manufacturing levels such as capital/piece cost, dimensional and sealing quality, and process flexibility to accommodate multi-variant vehicles on a single assembly cell. Blendl and Cuppoletta [2] recently reported that the use of 6xxx aluminium extruded profiles will rapidly increase from current level of ~20 kg used in the internal combustion engine vehicles to up to 250 kg. The projected rapid increase in the use of 6xxx aluminium extruded profiles for battery trays is motivated by its number of design advantages such as (i) very good corrosion resistance; (ii) lightweight with good material strength through heat treatment and ageing; (iii) excellent formability which enables design flexibility and modularity; and, (iv) overall relatively low material cost [3,4].

On the other hand, the selection of joining process presents a number of challenges [5]. For example, the environmental vulnerability and high sensitivity to the loading direction for adhesive bonding [6,7] and the uneven stress distribution and concentration at threads for mechanical fastening [8,9]. Remote laser welding (RLW) is emerging as a powerful and promising joining technology, which can easily create joints in different locations of the product through simple robot repositioning and/or laser beam redirection from a remote distance [10]. RLW demonstrates remarkable high processing flexibility and welding speed gained from rapid response of laser scanner optics. Additionally, it has a lower operational cost as it does not require filler wire and shielding gas [4,11–13]. It has been successfully deployed in a number of lightweight applications in automotive industry such as AA5182 doors [14] and AC-170PX outer skin panel [15]. However, efficient application of RLW for 6xxx aluminium extrusion profiles remains a challenge due to the formation of hot cracking, thus limiting the industry's ability to take full advantage of the spectrum of benefits provided by RLW. For instance, in case of battery tray construction, any crack generated during the welding process will act as a localised notch within the welded seam which can potentially propagate while the vehicle is in service, accelerated by vibrations and residual stresses. This, in turn, can severely reduce both, the structural integrity and service life of vehicle [16]. Therefore, it is important to understand the impact of cracks in RLW application for 6xxx aluminium extrusion as this will enable manufacturing aluminium intensive battery enclosures that can satisfy mass manufacturing requirements, accelerate transition to electric propulsion and meet requirement related to cost, weight and volume [17].

Hot cracking in the welding of aluminium alloy includes liquation cracking and solidification cracking [18]. Liquation cracking is induced by the re-melting of low melting alloy compounds and formation of brittle films on grain boundaries in the heat affected zone (HAZ). By comparison, solidification cracking occurs in the fusion zone when the molten material cools down just below the solidus temperature. In this paper, only solidification crack will be investigated since liquation cracks have rarely been observed due to the low heat input and narrow HAZ of laser welds [19]. As discussed by Hagenlocher et al. [20], solidification cracks in aluminium alloys are induced due to the presence of high thermal strain which exceeds the critical strength of semisolid material in the mushy zone and propagate along the continuous grain boundaries. Dudas [21] reported that the control of solidification cracking is challenging in the case of 6xxx aluminium alloys because the addition of Si content extends the critical solidification temperature range during rapid cooling period after welding. As reported in our previous study [22], solidification crack can be divided into centreline macro crack and transverse micro crack according to spatial distribution and scale. Centreline macro crack generally propagates along the centreline of weld seam at millimetre-scale and is visible on the external surface. In comparison, transverse micro crack is defined as internal or sub-surface crack at micron-scale and is only detectable by non-destructive techniques or observation of cross-section after metallographic preparation. In general, transverse micro cracks are found near the boundary between fusion zone and HAZ where local grains exhibit columnar structures. This is attributed to: (i) higher level of localised strains near the boundary of fusion zone [23]; and, (ii) higher crack susceptibility of columnar grains compared to equiaxed grains in the centre of fusion zone due to the increased grain size and reduced number of grain boundaries [24]. Several technological and metallurgical approaches have been proposed to prevent solidification cracks in laser welding of 6xxx aluminium alloys. These include: (i) modification of chemical composition through the use of filler wires [25,26]; (ii) refinement of grain structure by means of magnetic stirring, laser beam oscillation and addition of alloying elements [19,24]; and, (iii) temporal modulation of thermal history provided by beam shaping and beam oscillation [27].

The effect and characterisation of transverse micro crack on weld performance during RLW process has been rarely reported. Langrieger et al. [28] reported the presence of transverse micro cracks in RLW of AA6082 with fillet lap joints and observed that cracks

formed initially at the rear area beside the molten pool and propagated subsequently to the middle and the side of weld seam. Furthermore, they concluded that the molten pool geometry has a strong influence on crack formation and beam oscillation can therefore, be an effective solution for crack mitigation which generates an elliptical molten pool with a high curvature at the tip of the fusion zone. Langrieger et al. [29] further discussed the formation of transverse micro crack by thermomechanical analysis and related the hot cracking susceptibility to the local maximum strain rate in the vicinity of weld pool.

As proposed in our previous research [22], fillet lap joint configuration is a preferred joint design not only because of the effective control of centreline macro crack but also due to the pronounced capability of optical seam tracking and consequently, the opportunity for in-process measurement of the part-to-part gap [12,14]. Franciosa et al. [12] developed a closed-loop part-to-part bonding architecture to adaptively select welding process parameters as a function of the part-to-part gap and achieve the desired level of bonding between parts being welded. The aforementioned work revealed that although bonding condition is necessary to guarantee seam continuity [22], it is not sufficient to understand the impact of transverse micro cracks on joint mechanical strength and fatigue durability, particularly in the fillet lap joint configuration. This is especially important for battery tray application which needs to satisfy water and gas tightness requirements [30].

The aim of this paper is to experimentally examine the impact of transverse micro cracks on the mechanical strength and fatigue durability of the remote laser welded AA6063 fillet lap joints for battery tray assembly. Both spatial beam oscillation and temporal laser power modulation were integrated with the laser welding system, and three key processing parameters: welding speed, beam oscillation frequency and laser power were considered. Distribution and morphology of transverse micro crack were acquired by scanning electron microscope (SEM) on cross-sections. Grain morphology in the weld zone was determined by electron backscatter diffraction (EBSD). Furthermore, mechanical tests including static tensile and dynamic fatigue tests were carried out to evaluate weld mechanical performance and fatigue durability.

2. Materials and Methods

2.1. Welding Procedures

The material used in this paper was 1.45 mm thick AA6063-T6 extrusion (nominal compositions in Table 1, measured by Foundry-Master Pro2 optical emission spectrometer), which was machined into 150 mm x 55 mm coupons. A 6 kW diode laser (LaserLine GmbH, Mülheim-Kärlich, Germany) with a beam parameter product of 6 mm·mrad was used. The laser beam was delivered through an optical fibre of 150 µm diameter and coupled with the WeldMaster remote welding head (YW52 Precitec GmbH, Gaggenau, Germany), which has the collimating length of 150 mm and focal length of 300 mm. The resulting Rayleigh length is 2.8 mm.

Table 1. Nominal compositions of AA6063-T6, measured by Foundry-Master Pro2 optical emission spectrometer.

Chemical Composition Limits									
Weight %	Si	Fe	Cu	Mn	Mg	Zn	Ti	Cr	Al
Minimum	0.2	-	-	-	0.45	-	-	-	Balance
Maximum	0.6	0.35	0.1	0.1	0.9	0.1	0.1	0.1	Balance

Beam oscillation is achieved by the motorized mirror and collimator in the laser welding head in the form of cosine curve. Temporal power modulation is allowed by the analogue interface between the laser source and the laser welding head. Illustration of key welding parameters of beam oscillation and power modulation is shown in Figure 1. Process parameters are as follows: oscillation amplitude, A_y, of the cosine oscillation path with frequency f; lateral offset, O_y, measured from the reference point (defined by edge of

upper part), which defines the central position of oscillation pattern in the y direction; focal point position offset, A_Z, which corresponds the distance along the beam axis between the focused position and the top surface of upper part; laser power, P, which is modulated transversally to the welding direction on four points: P_A to P_D, corresponding to the laser power on the upper part (t = 0), reference point (t = 1/(4f)), lower part (t = 1/(2f)) and reference point (t = 3/(4f)). No shielding gas nor filler wire was used throughout the experiments. Samples were wiped with acetone before welding to remove surface contaminations.

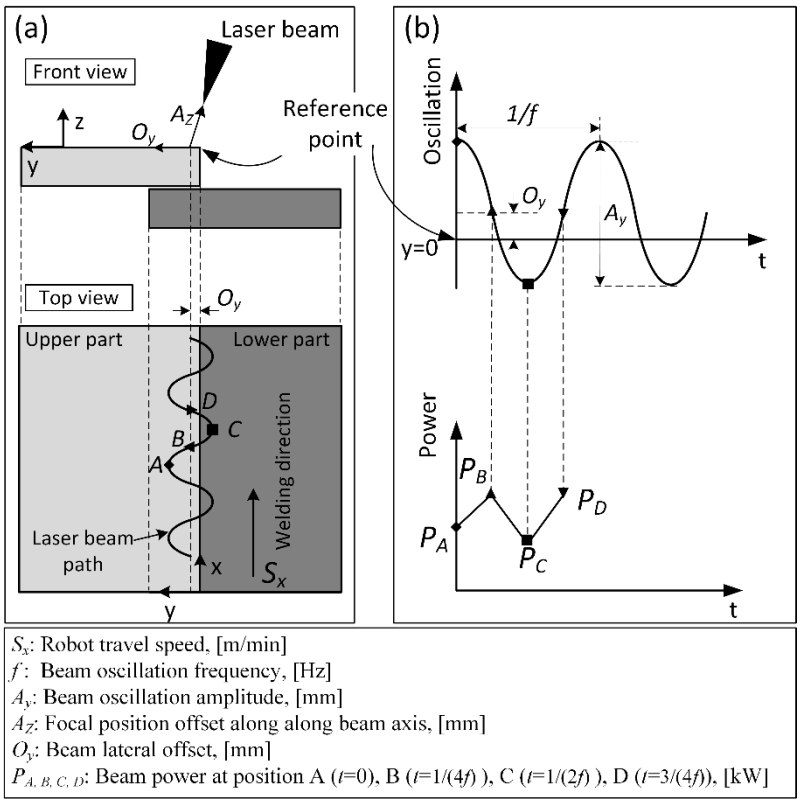

Figure 1. Illustration of key welding parameters. (**a**) Front view and top view showing the laser beam path; and (**b**) representation of beam oscillation and power modulation as function of time.

Full matrix of process parameters used in this paper is shown in Table 2. Three individual processing windows were studied in this paper which are defined by: (i) welding speed, S_x ranging from 2 m/min to 6 m/min; and (ii) the beam oscillation frequency, f which increases accordingly with S_x from 50 Hz to 150 Hz to maintain a constant cycle number over unit weld length. Selection of welding parameters at different welding speeds is based on the premise of good bonding between two parts, guided by previous research [12]. For all welding trials, a constant beam oscillation amplitude, A_y of 1.5 mm and focal offset, A_Z of 2.0 mm were employed. P_D was set to be same as P_B and omitted in the table. The line energy along the x direction, E_L is defined in Equation (1) using the average power across positions from A to D::

$$E_L = (P_A + P_B + P_C + P_D)/(4 * S_x), \ [\mathrm{J/mm}] \quad (1)$$

Figure 2 shows representative weld cross-sections obtained in each processing window and P_B was then further adjusted to extend the processing window.

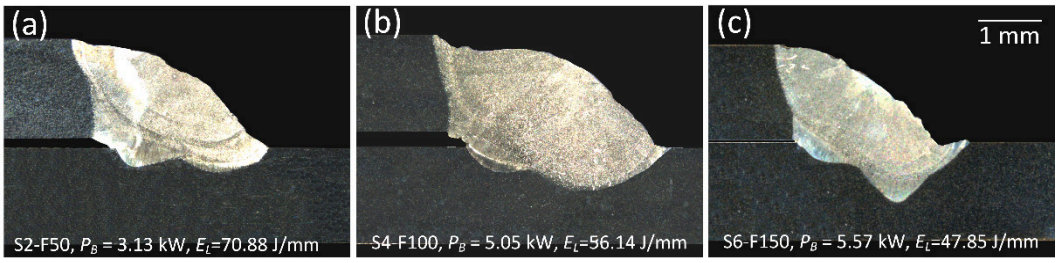

Figure 2. Representative weld cross-sections in the individual processing window (**a**) S2-F50, (**b**) S4-F100 and (**c**) S6-F150.

Table 2. Matrix of process parameters used in this paper.

Processing Window	S_x [m/min]	f [Hz]	O_y [mm]	P_A [kW]	P_B [kW]	P_C [kW]	Line Energy [J/mm]
S2-F50	2	50	0.4	1.74	3.25, 3.13, 2.90, 2.67	1.45	72.68, 70.88, 67.43, 64.07
S4-F100	4	100	0.7	2.55	5.28, 5.05, 4.81, 4.59	2.32	57.86, 56.14, 54.34, 52.69
S6-F150	6	150	0.3	4.52	5.80, 5.57, 5.34, 5.10	3.48	49.00, 47.85, 46.70, 45.50

2.2. Weld Morphology Characterisation

To obtain optical macro view of weld zone, samples were sectioned normal to the welding direction in the transverse-normal (y-z) plane and prepared metallographically by polishing to a 0.05 µm surface finish, followed by etching in caustic sodium fluoride reagent (2% NaOH + 5%NaF + 93% water). Electron backscatter diffraction (EBSD) was carried out in a JEOL 7800F SEM with a step size of 3 µm and accelerating voltage of 20 kV to investigate the grain morphology in the weld zone. The EBSD data acquisition was performed using the Aztec HKL EBSD software platform and then processed by HKL Channel 5 software. Observation of micro crack on the transverse-normal cross section was performed using Zeiss Sigma VP field emission gun-scanning electron microscope (FEG-SEM) in backscattered electron (BSE) mode with an accelerating voltage of 20 kV and a working distance of 10 mm. The quantity and cumulative length of micro cracks for each welding conditions were collected from three longitudinal-transverse (x-y) cross sections.

2.3. Mechanical Characterization

To evaluate the effect of transverse micro crack on the mechanical performance of weld joint under various loading conditions at room temperature, both lap shear tensile and fatigue tests were employed along the transverse direction according to ISO standards [31,32]. Test specimen with the weld length of 30 mm was machined from the welded sheet. Lap shear tensile tests were carried out on Instron® 3360 tensile machine equipped with 30 kN load cell and repeated for four times at each welding condition at an extension rate of 1 mm/min. Maximum linear load (N/mm) was then extracted from the stress-strain curve to evaluate the tensile strength of welds. Fatigue tests were carried on Instron® 8872 fatigue test machine under load control mode, with the load ration of R = 0.1 at room temperature. A sinusoidal waveform with a frequency of 20 Hz was used. An averaged maximum linear load was first summarized from tensile tests among all welding conditions and then 50% and 40% of this averaged load were employed to evaluate the fatigue performance.

3. Results and Discussion

3.1. Weld Shape

Weld depth of fusion (D) and effective weld width at interface (W_E), as illustrated in Figure 3, are used as key geometrical features in this paper to evaluate the bonding integrity between two parts. D was measured from the top surface of lower part to the root of the fusion zone and W_E was represented by the accumulated width of the intersection between the fusion zone and the top surface of the lower part. Acceptance limits on D and W_E, i.e., D greater than 10% of lower part thickness; and, W_E greater than the summation of lower

part thickness and part-to-part gap, have been adapted from international standards [33] to guarantee the minimum bonding condition at the interface between the parts being welded. For each processing window as shown in Table 2, increasing laser power (and consequently the line energy) leads to a wider and deeper fusion zone. However, not all the processing windows meet the bonding condition. For example, welding sets with low line energy in S6-F150 and S2-F50 exhibit insufficient W_E which indicates insufficient bonding area between top and bottom part (Figure 3b).

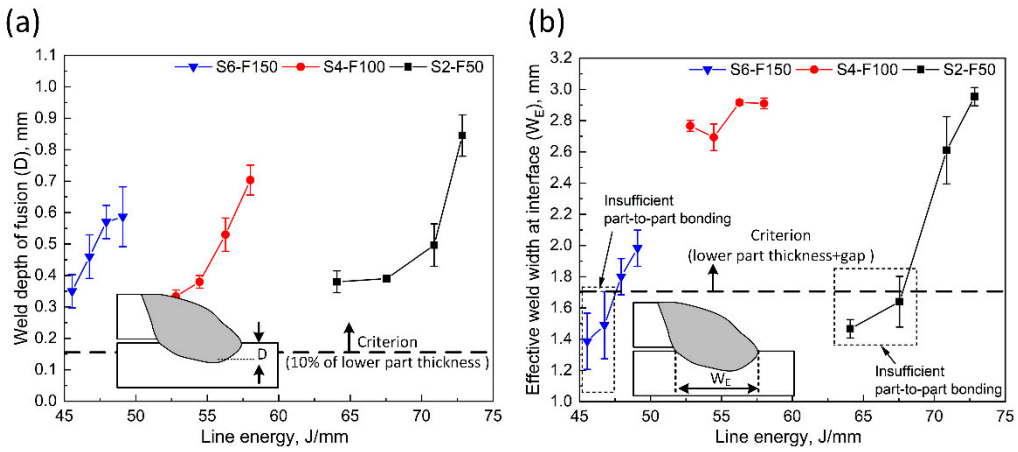

Figure 3. Evaluation of weld shape as function of welding parameters. (**a**) Weld depth of fusion and (**b**) effective weld width at interface.

3.2. Weld Zone Grain Morphology

Representative grain morphology maps at various welding speeds were determined by EBSD and shown in Figure 4. All weld cross-sections show both equiaxed grains in the centre and columnar grains near fusion lines. The growth of columnar grains is mainly along two directions due to the directional heat conduction during cooling stage: first, it is along the vertical direction from the bottom part to the fusion zone and secondly it develops horizontally from the upper part towards the weld centre. The formation of equiaxed grains in the weld centre is attributed to two phenomena:

(i) the energy flux distribution of an oscillated laser beam (Figure 5), $E(x, y)$, computed by Equation (2) [34] shows a 'M' shape in the transverse direction, with the peak energy deposition at two turning points of the oscillation path.

$$E(x,\ y) = \int_0^T P(t) exp\left\{-2 * \left[(x - x(t))^2 + (y - y(t))^2\right]/r^2\right\} dt,\ [\mathrm{J}] \tag{2}$$

where *P(t)* is the time-dependent instant power of laser beam expressed in Figure 1, *r* (r = 0.16 mm) is the radius of laser beam at A_z = 2 mm. *x(t)* and *y(t)* are the moving track of oscillating beam and can be expressed by Equations (3) and (4), respectively.

$$x(t) = S_x * t,\ [\mathrm{mm}] \tag{3}$$

$$y(t) = A_y * \cos(2\pi f t)/2,\ [\mathrm{mm}] \tag{4}$$

As confirmed by Jiang et al. [35], transverse oscillating welding introduces a wider molten pool and more uniform temperature gradient (G) in the fusion zone compared to rectilinear welding, which is favourable for the formation of equiaxed grains based on the solidification theory proposed by Kurz and Fisher [36].

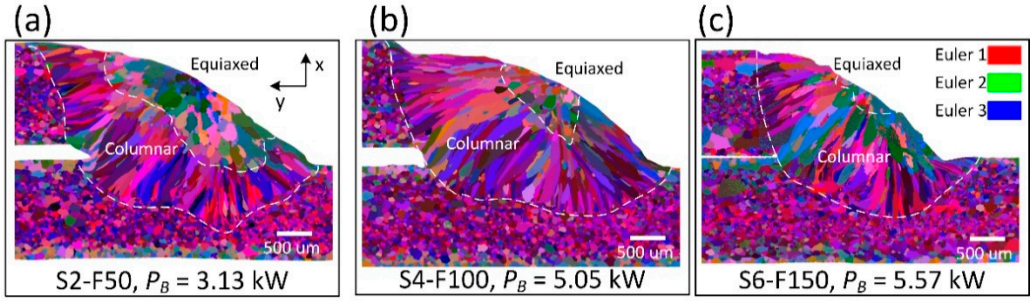

Figure 4. Representative EBSD Euler maps showing the grain structures of equiaxed and columnar grains in the weld zone of joint produced in processing windows (**a**) S2-F50; (**b**) S4-F100; and, (**c**) S6-F150.

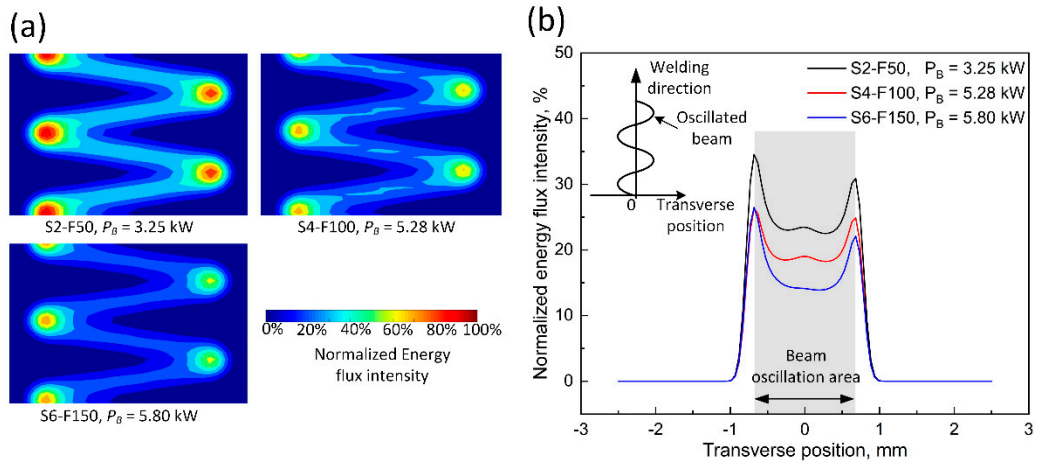

Figure 5. (**a**) Computed energy flux distribution on material surface in each processing window and (**b**) distribution of averaged energy flux intensity along transverse position. Note that energy flux intensity was calculated with Equation (2) normalised by the maximum E(x, y) among three processing windows.

(ii) the turbulence of molten material in the rear of the molten pool which is induced by the beam oscillation, disturbs the growth of columnar grains in the mushy zone and promote the formation of equiaxed grains. However, this stirring effect induced by transverse beam oscillation is relatively weak as compared to longitudinal and circular oscillations because the oscillations occur only in front of the molten pool [34].

Distribution of the size of columnar grain expressed by the length of major axis from elliptical fitting and total area of equiaxed grains are plotted in Figure 6. It is interesting to see that a lower welding speed facilitates the growth of equiaxed grains while suppresses the formation of columnar grains. Regarding the energy flux distribution (Figure 5), it is reasonable to infer that the evolution of grain morphology with reduced welding speeds is attributed to the higher energy deposition at the two edges of fusion zone (Figure 5b), which works as a stronger thermal barrier near the boundary of fusion and leads to a lower temperature gradient (G) within the fusion zone during subsequent solidification process [4]. Modelling work in [4,34,35] also confirmed the presence of a reduced G within the fusion zone as the energy deposition at two edges of fusion zone increases, which results in a larger constitutive undercooling region of the molten material and promotes the formation of equiaxed grains.

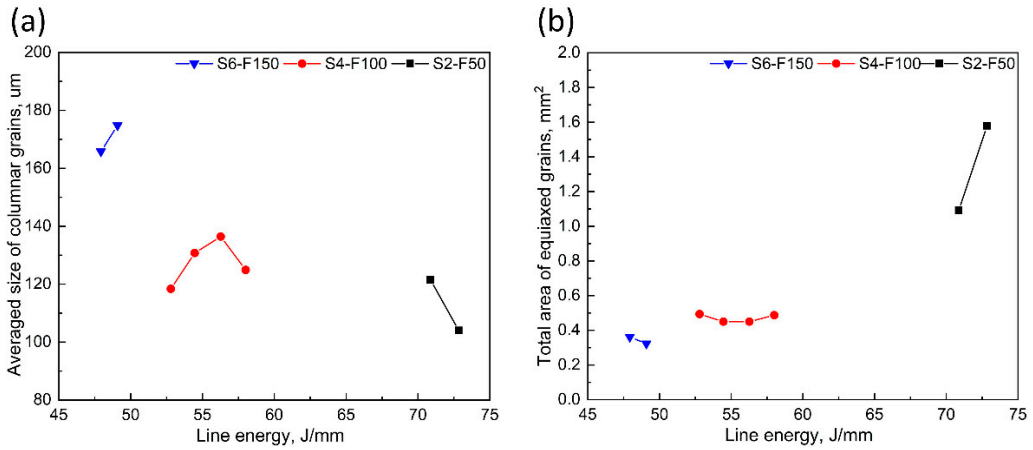

Figure 6. Distributions of (**a**) averaged grain size (length) of columnar grains and (**b**) total area of equiaxed grains in the weld zone as function of welding parameters, obtained from EBSD grain morphology maps. Note that welds with insufficient part-to-part bonding are not included.

3.3. Crack Distribution

Figure 7 shows the representative morphology of micro cracks from weld cross-sections. Micro cracks are distributed along grain boundaries of columnar grains near the fusion lines rather than equiaxed grains in the centre of fusion zone. This can be explained as follows: first, a higher localized thermal gradient and resultant thermal strain are generally found in the region adjacent to the boundary of weld zone where columnar grains distribute [23,37] and this is more obvious at the root of fusion zone because the entire lower part can work as "heat sink" for the molten droplet and cools down the fusion zone faster. Next, as the formation of micro crack is associated with the tearing of low melting eutectics along grain boundaries during final stage of solidification [38], equiaxed grains allow a distribution of thermal strain across more grain boundaries and also a reduced thickness of low melting eutectics on grain boundaries [39].

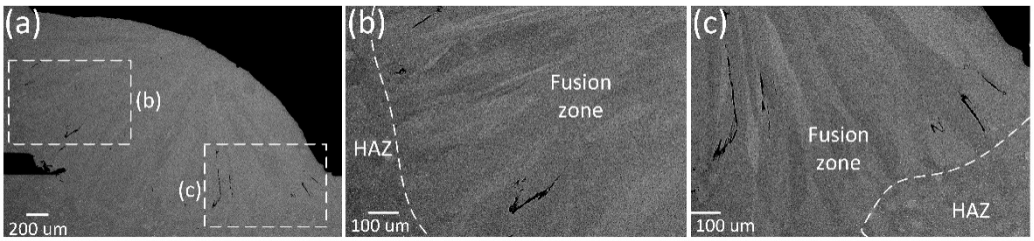

Figure 7. (**a**) SEM images taken in the weld zone of S2-F50 at P_B = 3.25 kW showing representative view of micro cracks. (**b**,**c**) show detailed distribution of micro cracks along the grain boundaries of columnar grains.

Figure 8 reports the evolution of cumulative total length of micro cracks and averaged length of individual micro crack on transverse cross-section in each processing window, measured by SEM over three cross-sections of each weld. In addition, the grey symbol represents the averaged level of micro cracks in each process window. Overall, it is evident that micro crack in RLW of AA6063 fillet lap joints cannot be eliminated by the optimisation of welding speed. One-way ANOVA with the significance level of 0.05 has showed *p*-value of ~0.68 and ~0.65 for test of welding speed on the total length and individual length. This result confirms that increasing welding speed in the sample will not induce additional risk of transverse micro cracks, in terms of total length and averaged individual length of cracks. Although less equiaxed grains and greater scale of columnar grains have been observed in welds with higher welding speed, which is favourable for the formation of crack, it is likely that the lower residual stress near the fusion zone due to a reduced line

energy [40] compensates the possibility of crack formations. In addition, for the process window of S6-F150 and S4-F100, there tends to be a sudden increase in the total/averaged length of crack at the line energy of 47 J/mm and 55 J/mm respectively. This is possibly due to the promotion of part-to-part bonding as illustrated in Figure 3, and resultant heat transfer between two parts that first narrows the region with undercooling, facilitating the formation of columnar grains (Figure 6) and secondly accelerates the cooling stages and development of thermal strain [37], which are favorable for the formation of micro crack.

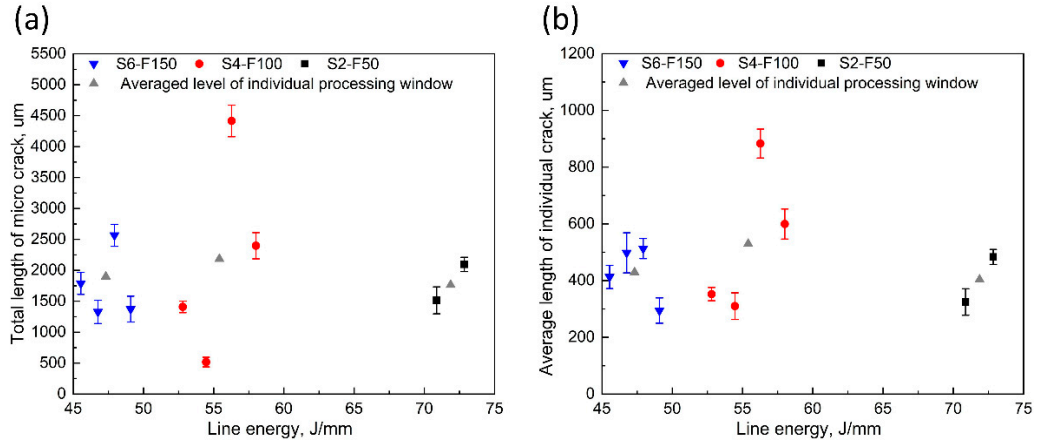

Figure 8. Distribution of (**a**) total length of all cracks and (**b**) average length of individual crack as function of welding parameters, measured by SEM on cross-sections with three replications at different positions along the welding directions for each welding condition. Grey dashed line represents the averaged level of individual processing window.

3.4. Weld Tensile Strength and Fatigue Durability

To evaluate the effect of micro crack on weld mechanical performance, tensile lap shear test was performed along the transverse direction. Fusion zone failure was determined in all welding conditions and the failure initiates from the internal toe between the two parts and grows through the top part at an angle of around 45 degree (see Figure 9a,b). Interestingly, the failure position agrees with previous work [41] on fillet lap RLW joints of AA5182 sheet metal components. However, those welds were not prone to micro cracks because of the nature of the AA5182 alloy. This indicates that the transverse micro crack is not the root cause of failure position at the internal toe and instead it is the localised strain concentration at the internal toe that promotes the initiation of failure. The strain concentration is believed to be attributed to two factors: (i) loss of material strength in the fusion zone due to the large columnar grain structure according to the Hall-Petch relationship and evolution of the strengthening precipitates [22]; and (ii) stress concentration at the edge of bonding area resulting from the structural nature of fillet lap configuration during the tensile shear loading [42].

The representative tensile fractography from three individual processing window is shown in Figure 9c,e,g. Large cavities observed on each fractography confirm the existence of micro cracks. Furthermore, a non-uniform fracture morphology was captured (Figure 9d,f,h), where small dimples in Region 1 (highlighted by dashed box) indicates the ductile fracture features and facets in Region 2, (highlighted by solid box) confirms the cleavage fracture near micro cracks. These fracture features revealed that transverse micro crack facilitates the rapid propagation of tensile failure and degrades the joint strength. Though reducing welding speed shows no obvious impact on the mitigation of micro crack, Figure 8, there is still an apparent improvement in joint tensile strength as shown in Figure 10. This is attributed to two phenomena: firstly, an increase in the throat thickness of fusion zone results in a larger effective bonding area (black box in Figure 11b and hence, greater resistance to the tensile shear. Secondly, the refinement of the columnar grains

(red triangle in Figure 11b) adjacent to the failure position improves the localised material strength [43].

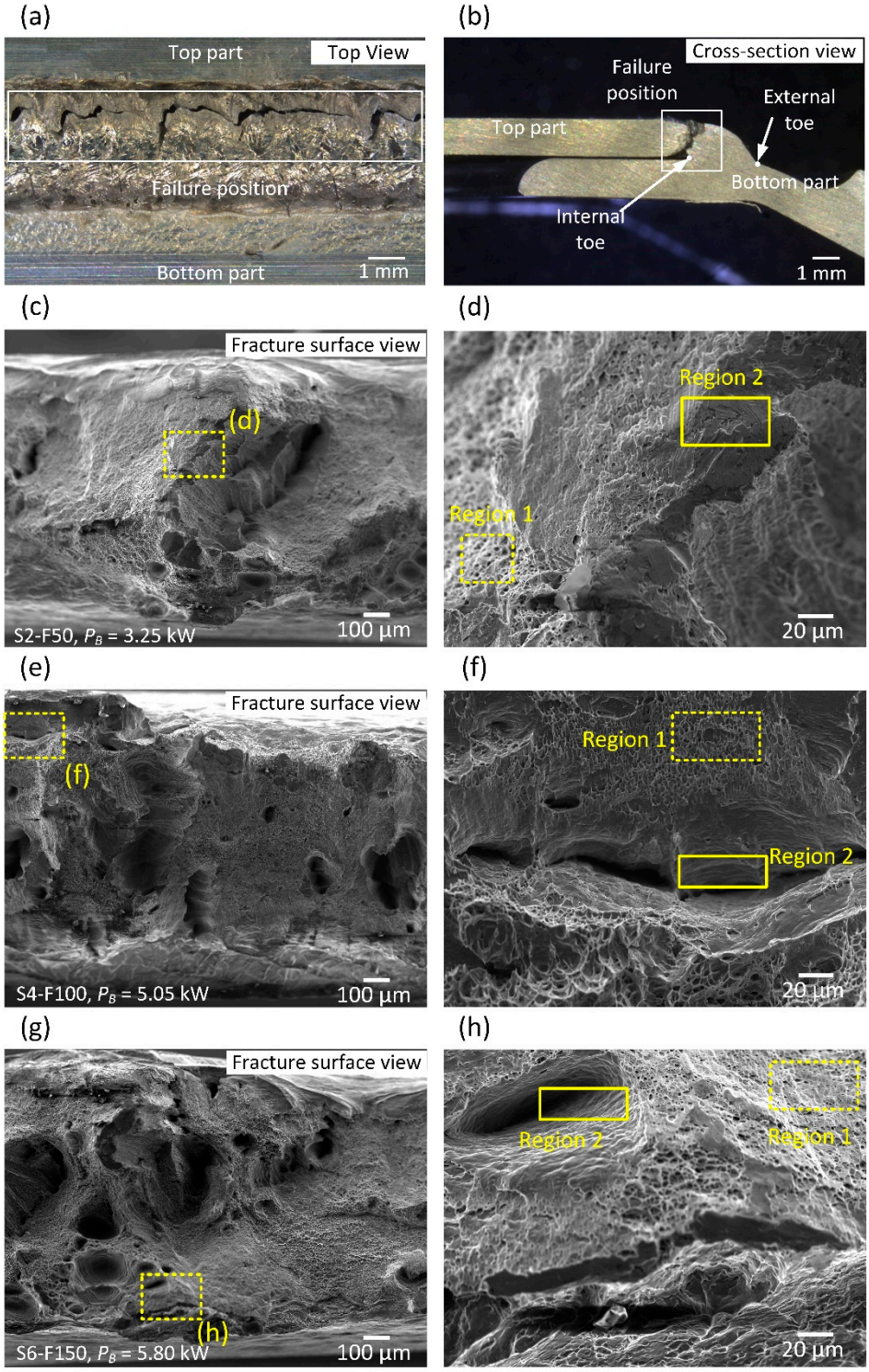

Figure 9. Representative (**a**) top view and (**b**) cross-section view of the failure position during tensile test by optical microscopy; representative fracture morphology of welds by SEM in the processing window of (**c**) S2-F50, (**e**) S4-F100 and (**g**) S6-F150, with the high magnification view in (**d**,**f**,**h**), respectively.

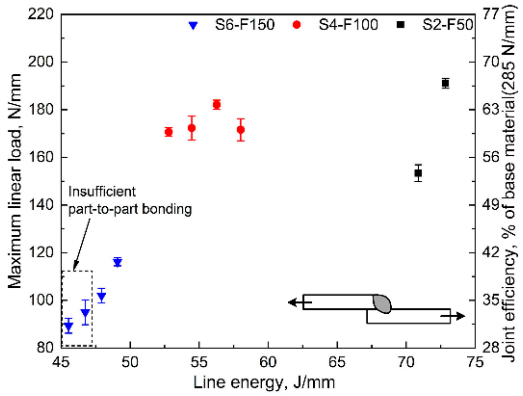

Figure 10. Maximum linear load during lap shear tensile test as function of welding parameters.

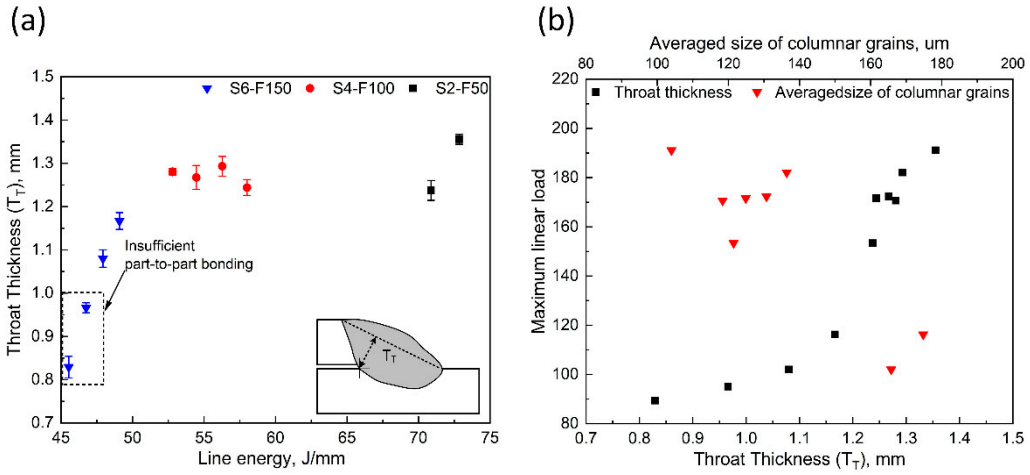

Figure 11. (**a**) Maximum linear load during tensile test and; (**b**) weld zone throat radius as function of welding parameters.

Fatigue test was then employed to investigate the effect of micro crack on joint fatigue durability. An averaged maximum linear load of welds among three processing windows was first calculated and then both 40% and 50% of this averaged maximum linear load were used as the peak load in the fatigue test with load ration of R = 0.1. Overall, weld root failure was observed in the processing window of S4-F100 and S6-F150 while fusion zone failure was found in the process window of S2-F50. Figure 12a–d shows the representative top view and cross-section view of the fatigue fractured section in each failure mode. For the fusion zone failure, the fatigue fatal crack originally initiated in the fusion zone adjacent the internal toe, which composed of columnar microstructure as shown in magnified figure (Figure 12e) and propagates along the grain boundary. In comparison, fatigue fatal crack in the weld root failure mode initiated at the boundary between the columnar microstructure and equiaxed microstructure and propagates vertically into HAZ. Though differing from the failure location, fatal crack initiates at boundary of columnar grains in both failure modes. As the resistance to crack initiation in the high cycle fatigue (HCF) regime depends primarily on the resistance to dislocation motion, the HCF strength consequently relies on the yield strength which increases with reduced grain size, leading to a weak point at the columnar grain. The discrepancy in failure position between the tensile test and fatigue test for S4-F100 and S6-F150 may be attributed to different test conditions including the load level and strain rate. These differences are likely to amplify the impact of stress concentration, resulting from the geometrical nature of fillet lap joint [42], on the failure position during fatigue test, which may even overcome the weaken effect of micro cracks observed in the fusion zone (shown in Figure 12g–i). Shiozaki et al. [44] reported that

a smoother weld external toe can greatly mitigate the stress concentration which makes the internal toe more favourable for stress concentration. Therefore, transition of the failure mode from weld root failure (S4-F100 and S6-F150) to fusion zone failure (S2-F50) is observed in this study as the root angle decreases (Figure 13). This type of transition of failure mode was also reported in a study by Bergmann and Herold [45].

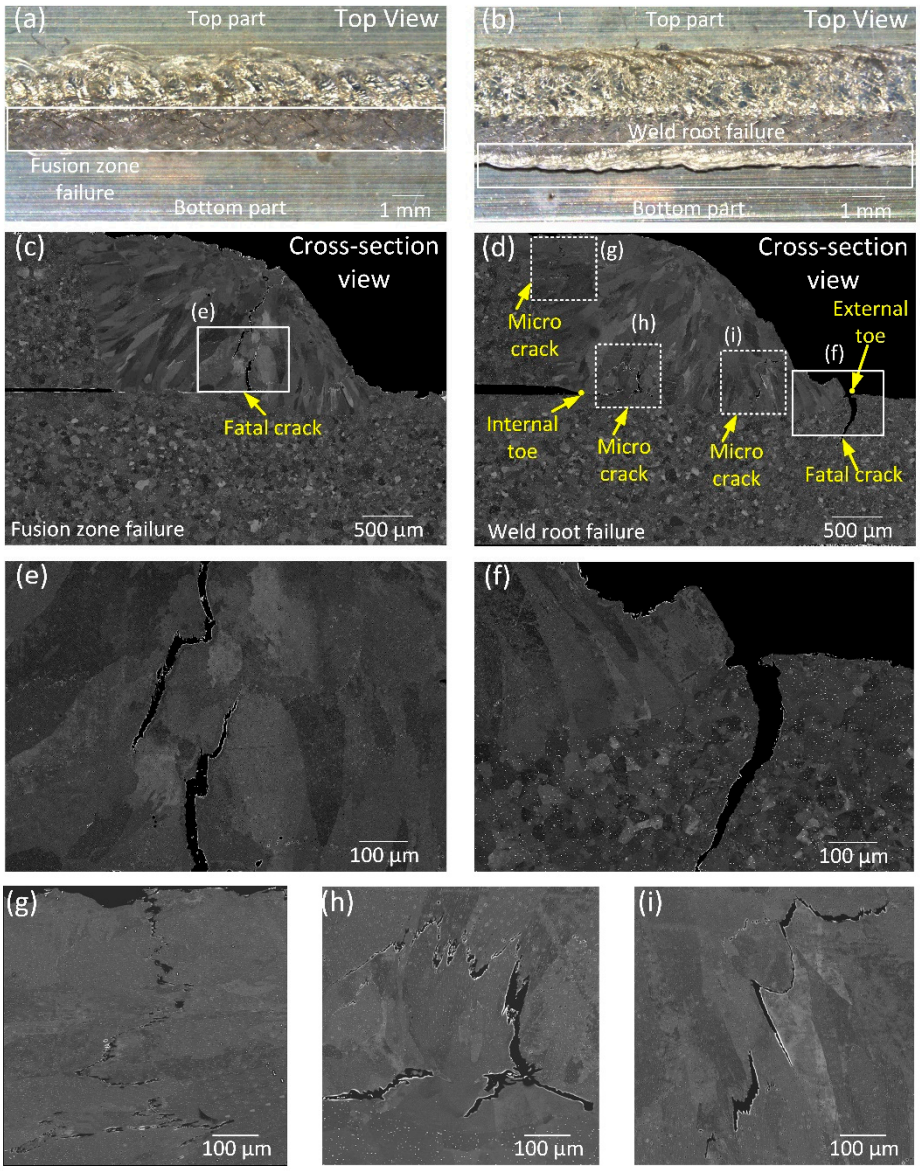

Figure 12. Representative top view (**a**,**b**) and cross section view (**c**,**d**) of fatigue failure in fusion zone and weld root respectively with detailed view near the fatigue fatal crack in (**e**,**f**). (**g**–**i**) show the high magnification view of transverse micro crack in positions addressed in (**d**). (**a**,**c**) were obtained from S6-F150 at P_B = 5.57 kW. (**b**,**d**) were obtained from S2-F50 at P_B = 3.25 kW.

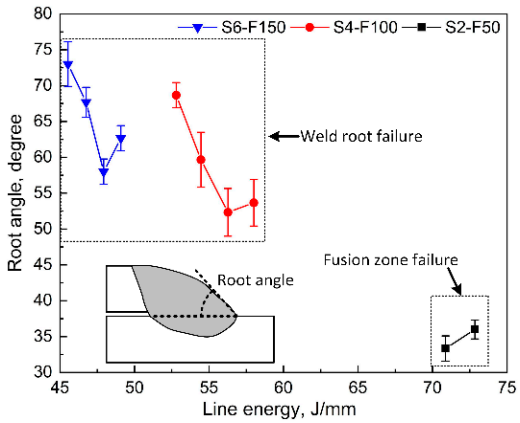

Figure 13. Distribution of weld root angle as function of welding parameters.

Fatigue cycles, as functions of welding parameters and weld root angles, are plotted in Figure 14. Results indicate an improvement in fatigue durability when fracture occurs in weld root failure mode instead of fusion zone failure mode. Furthermore, for those welds in the weld root failure mode, a peak fatigue performance was observed at the root angle at around 55 degrees. Further increases of root angle reduced the fatigue durability due to excessive stress concentration in the external toe. To better understand significant difference in the fatigue durability between two failure modes, fatigue fractured surface was studied utilizing SEM. Figure 15a,c show the representative fracture surface of fusion zone failure and weld root failure, respectively. It is evident in the magnified image (Figure 15b) that micros crack and pores near the internal toe (as indicated by the large cavity) facilitate the rapid propagation of fatal crack failure the columnar grain boundary and consequently result in a brittle characteristic. In comparison, a smooth fracture surface was determined in the weld root failure, without obvious sign of micro cracks. It should be noted that in addition to the avoidance of micro crack near the fatal crack, the reduced size of the extruded grain structure in HAZ, compared to the columnar grain in the fusion zone, and the resultant higher localised material strength are also beneficial for the enhancement of fatigue durability [43].

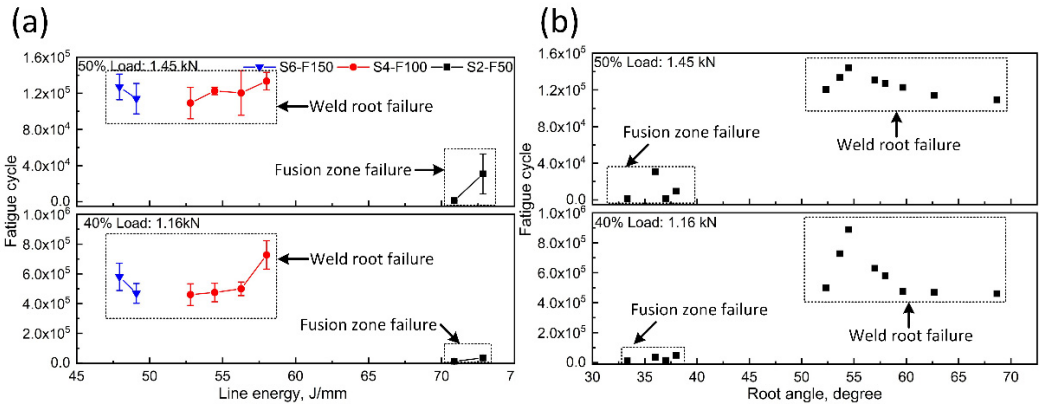

Figure 14. (**a**) Distribution of fatigue failure cycles at 50% load (1.45 kN—top chart) and 40% load (1.16 kN—bottom chart) as a function of welding parameters, grouped with two types of failure mode and (**b**) relationship between the fatigue failure cycles and weld root angle, showing the significantly improved fatigue performance in the weld root failure mode, with the maximum fatigue cycle at the root angle about 55°.

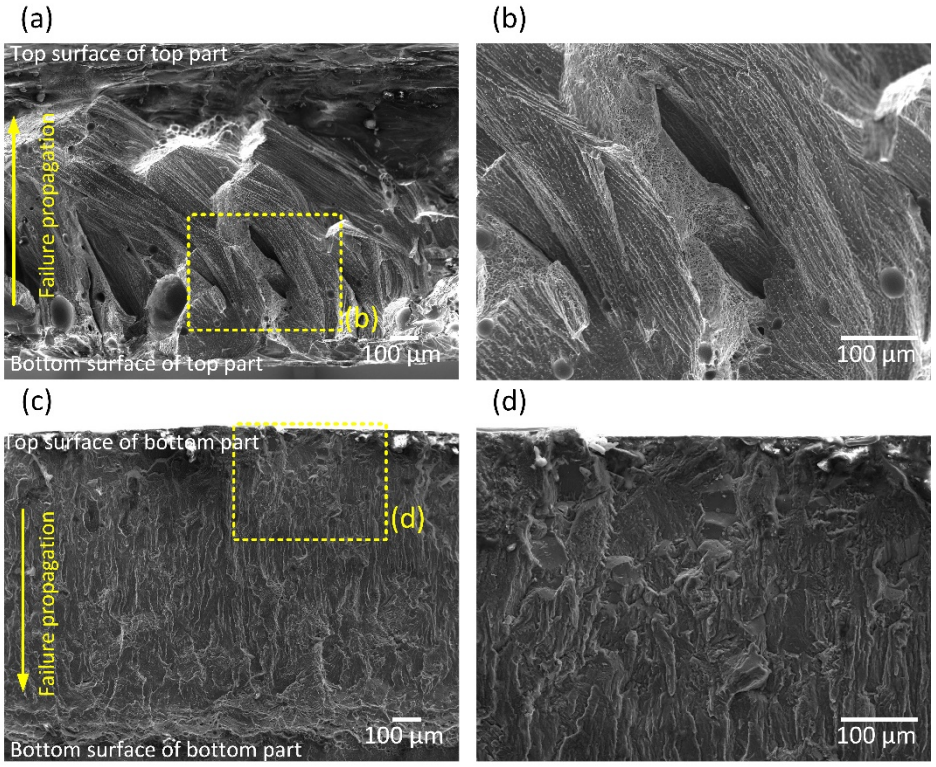

Figure 15. Representative fatigue fractography of (**a**) the fusion zone failure and (**c**) the weld root failure, with detailed views in (**b**) and (**d**).

4. Conclusions

This paper investigated the impact of transverse micro solidification cracks in remote laser welding of AA6063-T6 fillet lap joint at different welding speeds with consideration to part-to-part bonding, laser beam oscillation and power modulation. Results show that:

(1) Transverse micro cracks occur along the columnar grain boundaries near fusion lines. Increasing welding speed from 2 m/min to 6 m/min, simultaneously with an increasing laser power for the purpose of good part-to-part gap bridging, did not show any risk of introducing additional transverse micro cracks.

(2) Equiaxed grains were observed in the centre of fusion zones while columnar grains were determined near fusion lines. A reduced welding speed facilitates the formation of equiaxed grains due to the greater deposition of beam energy at two turning points of the beam oscillation path, which results in a more uniform temperature distribution within the fusion zone during subsequent solidification.

(3) Although transverse micro crack remains at similar level for welding speed between 2 m/min and 6 m/min, joint tensile strength can be improved by 30% by welding at 2 m/min compared to 6 m/min. This is attributed to expansion of fusion zone, measured by throat thickness and refinement of columnar grains near fusion lines.

(4) Weld fatigue durability is higher when fatigue failure occurs in weld root instead of fusion zone due to the avoidance of transverse micro cracks. Weld fatigue failure position in this study is greatly influenced by weld shape, represented by weld root angle. A higher weld root angle leads to the transition of fatigue failure from the centre of fusion zone (fusion zone failure mode) to the interface between fusion zone and HAZ (weld root failure mode). The highest weld fatigue durability can be achieved by increasing weld root angle with optimum weld fatigue durability at weld root angle of around 55°.

In order to harness the full benefits of remote laser welding at higher speeds (>2 m/min) compared to tactile laser welding and achieve significant reduction in number of transverse micro cracks, future research will explore RLW with dual laser beam to achieve a localised

control of the thermal field (both heating and cooling stage) and grain structure refinement in the fusion zone.

Author Contributions: Conceptualization, T.S. and P.F.; methodology, T.S. and P.F.; investigation, T.S., C.L., F.P. and P.F.; writing—original draft preparation, T.S.; writing—review and editing, all authors; supervision, P.F. and D.C.; funding acquisition, P.F. and D.C. All authors have read and agreed to the published version of the manuscript.

Funding: This study was partially supported by the WMG HVM Catapult, APC UK project: Chamaeleon—New lightweight Materials and Processing Technologies for Common Lightweight Architecture of Electric and Hybrid Powertrain Systems, and the Innovate UK IDP15 Project LIBERATE: Lightweight Innovative Battery Enclosures using Recycled Aluminium Technologies.

Institutional Review Board Statement: Not applicable.

Informed Consent Statement: Not applicable.

Data Availability Statement: The data supporting this research article are available upon request to the corresponding authors.

Acknowledgments: Tianzhu Sun would like to thank Paul Hadlum for the enthusiastic support at WMG Materials testing laboratory.

Conflicts of Interest: The authors declare no conflict of interest.

References

1. González Palencia, J.C.; Furubayashi, T.; Nakata, T. Energy use and CO2 emissions reduction potential in passenger car fleet using zero emission vehicles and lightweight materials. *Energy* **2012**, *48*, 548–565. [CrossRef]
2. Blendl, W.; Cuppoletta, N. Trend Towards e-Mobility Accelerates Aluminium Use. 2020. Available online: https://www.aluminium-messe.com/en/ALUMINIUM-2020/Trend-towards-e-Mobility-accelerates-Aluminium-Use/879/ (accessed on 20 December 2020).
3. Pedersen, K.O.; Lademo, O.G.; Berstad, T.; Furu, T.; Hopperstad, O.S. Influence of texture and grain structure on strain localisation and formability for AlMgSi alloys. *J. Mater. Process. Technol.* **2008**, *200*, 77–93. [CrossRef]
4. Zhang, C.; Li, X.; Gao, M. Effects of circular oscillating beam on heat transfer and melt flow of laser melting pool. *J. Mater. Res. Technol.* **2020**, *9*, 9271–9282. [CrossRef]
5. Bustillo, A.; Urbikain, G.; Perez, J.M.; Pereira, O.M.; Lopez de Lacalle, L.N. Smart optimization of a friction-drilling process based on boosting ensembles. *J. Manuf. Syst.* **2018**, *48*, 108–121. [CrossRef]
6. Khosravani, M.R.; Anders, D.; Weinberg, K. Influence of strain rate on fracture behavior of sandwich composite T-joints. *Eur. J. Mech. A Solid* **2019**, *78*, 103821. [CrossRef]
7. Khosravani, M.R.; Weinberg, K. Experimental investigations of the environmental effects on stability and integrity of composite sandwich T-joints. *Materwiss. Werksttech.* **2017**, *48*, 753–759. [CrossRef]
8. Zhou, W.; Zhang, R.; Ai, S.; He, R.; Pei, Y.; Fang, D. Load distribution in threads of porous metal–ceramic functionally graded composite joints subjected to thermomechanical loading. *Compos. Struct.* **2015**, *134*, 680–688. [CrossRef]
9. Zhou, W.; Ai, S.; Chen, M.; Zhang, R.; He, R.; Pei, Y.; Fang, D. Preparation and thermodynamic analysis of the porous ZrO_2/(ZrO_2+Ni) functionally graded bolted joint. *Compos. Part B Eng.* **2015**, *82*, 13–22. [CrossRef]
10. Ceglarek, D.; Colledani, M.; Váncza, J.; Kim, D.Y.; Marine, C.; Kogel-Hollacher, M. Rapid deployment of remote laser welding processes in automotive assembly systems. *CIRP Ann. Manuf. Technol.* **2015**, *64*, 389–394. [CrossRef]
11. Tsoukantas, G.; Salonitis, K.; Stournaras, A.; Stavropoulos, P.; Chryssolouris, G. On optical design limitations of generalized two-mirror remote beam delivery laser systems: The case of remote welding. *Int. J. Adv. Manuf. Technol.* **2007**, *32*, 932–941. [CrossRef]
12. Franciosa, P.; Serino, A.; Botros, R.A.; Ceglarek, D. Closed-loop gap bridging control for remote laser welding of aluminum components based on first principle energy and mass balance. *J. Laser Appl.* **2019**, *31*, 022416. [CrossRef]
13. Li, L.; Gong, J.; Xia, H.; Peng, G.; Hao, Y.; Meng, S. Influence of Scan Paths on Flow Dynamics and Weld Formations during Oscillating Laser Welding of 5A06 Aluminum Alloy. *J. Mater. Res. Technol.* **2020**, *11*, 19–32. [CrossRef]
14. Franciosa, P.; Sokolov, M.; Sinha, S.; Sun, T.; Ceglarek, D. Deep learning enhanced digital twin for Closed-Loop In-Process quality improvement. *CIRP Ann. Manuf. Technol.* **2020**, *69*, 369–372. [CrossRef]
15. Das, A.; Butterworth, I.; Masters, I.; Williams, D. Evaluation of key geometrical and mechanical properties for remote laser welded AC-170PX aluminium joints. *J. Laser Micro. Nanoeng.* **2019**, *14*, 1–7. [CrossRef]
16. ISO 20653:2013. *Road Vehicles-Degrees of Protection (IP code)-Protection of Electrical Equipment against Foreign Objects, Water and Access*; International Organization for Standardization: Geneva, Switzerland, 2013.
17. Graf, A. Aluminum alloys for lightweight automotive structures. In *Materials, Design and Manufacturing for Lightweight Vehicles*; Woodhead Publishing: Cambridge, UK, 2021; pp. 97–123. [CrossRef]

18. Ghaini, F.M.; Sheikhi, M.; Torkamany, M.J.; Sabbaghzadeh, J. The relation between liquation and solidification cracks in pulsed laser welding of 2024 aluminium alloy. *Mater. Sci. Eng. A* **2009**, *519*, 167–171. [CrossRef]
19. Zhao, H.; White, D.R.; Debroy, T. Current issues and problems in laser welding of automotive aluminum alloys. *Int. Mater. Rev.* **1999**, *44*, 238–266. [CrossRef]
20. Hagenlocher, C.; Weller, D.; Weber, R.; Graf, T. Analytical description of the influence of the welding parameters on the hot cracking susceptibility of laser beam welds in aluminum alloys. *Metall. Mater. Trans. A Phys. Metall. Mater. Sci.* **2019**, *50*, 5174–5180. [CrossRef]
21. Dudas, H.J. Preventing weld cracks in high strength aluminum alloys. *Weld. J.* **1966**, *45*, 3.
22. Sun, T.; Franciosa, P.; Sokolov, M.; Ceglarek, D. Challenges and opportunities in laser welding of 6xxx high strength aluminium extrusions in automotive battery tray construction. *Procedia CIRP* **2020**, *94*, 565–570. [CrossRef]
23. Wang, X.; Lu, F.; Wang, H.P.; Qu, Z.; Xia, L. Micro-scale model based study of solidification cracking formation mechanism in Al fiber laser welds. *J. Mater. Process. Technol.* **2016**, *231*, 18–26. [CrossRef]
24. Hagenlocher, C.; Weller, D.; Weber, R.; Graf, T. Reduction of the hot cracking susceptibility of laser beam welds in AlMgSi alloys by increasing the number of grain boundaries. *Sci. Technol. Weld. Join.* **2019**, *24*, 313–319. [CrossRef]
25. Guitterez, L.A.; Neye, G.; Zschech, E. Microstructure, hardness profile and tensile strength in welds of AA6013 T6 extrusions. *Weld. J.* **1996**, *75*, 4.
26. Alshaer, A.W.; Li, L.; Mistry, A. Effect of filler wire properties on porosity formation in laser welding of AC-170PX aluminium alloy for lightweight automotive component manufacture. *Proc. Inst. Mech. Eng. Part B J. Eng. Manuf.* **2017**, *231*, 994–1006. [CrossRef]
27. Kang, M.; Han, H.; Kim, C. Microstructure and solidification crack susceptibility of al 6014 molten alloy subjected to a spatially oscillated laser beam. *Materials (Basel)* **2018**, *11*, 648. [CrossRef]
28. Langrieger, H.; Krafft, F.; Mensinger, M.; Oefele, F. Fundamental analysis of hot cracks in remote laser welded aluminium fillet welds. In Proceedings of the Lasers in Manufacturing Conference (LiM), Munich, Germany, June 2015.
29. Langrieger, H.; Krafft, F.; Mensinger, M.; Oefele, F. Thermomechanical analysis of the formation of hot cracks in remote laser welded aluminium fillet welds. *J. Laser Appl.* **2016**, *28*, 022414. [CrossRef]
30. Gaisne, D.; Leclercq, J.-P. Battery Tray for Vehicle and Method for Producing the Battery Tray. U.S. Patent Appl. US13/509,453, 6 September 2012.
31. ISO 6892-1:2019. *Metallic Materials-Tensile Testing—Part 1: Method of Test at Room Temperature*; International Organization for Standardization: Geneva, Switzerland, 2019.
32. ISO 12106:2017. *Metallic Materials-Fatigue Testing-Axial-Strain-Controlled Method*; International Organization for Standardization: Geneva, Switzerland, 2017.
33. ISO EN13919-2. *Welding–Electron and Laser Beam Welded Joints–Guidance on Quality Levels for Imperfections—Part 2*; International Organization for Standardization: Geneva, Switzerland, 2001.
34. Wang, L.; Gao, M.; Zhang, C.; Zeng, X. Effect of beam oscillating pattern on weld characterization of laser welding of AA6061-T6 aluminum alloy. *Mater. Des.* **2016**, *108*, 707–717. [CrossRef]
35. Jiang, Z.; Chen, X.; Li, H.; Lei, Z.; Chen, Y.; Wu, S. Grain refinement and laser energy distribution during laser oscillating welding of Invar alloy. *Mater. Des.* **2020**, *186*, 108195. [CrossRef]
36. Kurz, W.; Fisher, D.J. *Fundamentals of Solidification*; Trans Tech Publications Ltd.: Aedermannsdorf, Switzerland, 1989.
37. Zain-ul-Abdein, M.; Nelias, D.; Jullien, J.F.; Deloison, D. Prediction of laser beam welding-induced distortions and residual stresses by numerical simulation for aeronautic application. *J. Mater. Process. Technol.* **2009**, *209*, 2907–2917. [CrossRef]
38. Sheikhi, M.; Malek Ghaini, F.; Torkamany, M.J.; Sabbaghzadeh, J. Characterisation of solidification cracking in pulsed Nd:YAG laser welding of 2024 aluminium alloy. *Sci. Technol. Weld. Join.* **2009**, *14*, 161–165. [CrossRef]
39. Tang, Z.; Vollertsen, F. Influence of grain refinement on hot cracking in laser welding of aluminum. *Weld. World* **2014**, *58*, 355–366. [CrossRef]
40. Zhan, Y.; Zhang, E.; Ge, Y.; Liu, C. Residual stress in laser welding of TC4 titanium alloy based on ultrasonic laser technology. *Appl. Sci.* **2018**, *8*, 1997. [CrossRef]
41. Serino, A. Development of Closed-Loop Gap Bridging Architecture for Remote Laser Welding of 5xxx Series Aluminium Alloy. Master's Thesis, University of Warwick, Coventry, UK, 2018.
42. Riggs, B.; Benatar, A.; Alexandrov, B.T.; Xu, R. Experimental validation of damage zone models for Lap-Shear brazed joints using DIC. *Weld. J. WRS* **2017**, 421–428.
43. Hansen, N. Hall-petch relation and boundary strengthening. *Scr. Mater.* **2004**, *51*, 801–806. [CrossRef]
44. Shiozaki, T.; Yamaguchi, N.; Tamai, Y.; Hiramoto, J.; Ogawa, K. Effect of weld toe geometry on fatigue life of lap fillet welded ultra-high strength steel joints. *Int. J. Fatigue* **2018**, *116*, 409–420. [CrossRef]
45. Bergmann, J.P.; Herold, S. Influence of processing conditions on the mechanical properties of aluminium overlap joints: A case study. *Weld. World* **2006**, *50*, 55–64. [CrossRef]